

Investigating the nanoscale hardness/strength properties of high-entropy alloy particles using the nanoindentation technique

Aisa Grace Custodio ^{a,b}, Klara Joy Lindquist ^a, Marvin Tolentino ^{a,b}, Clodualdo Aranas Jr. ^b, Gobinda C. Saha ^{a,*}

^a Nanocomposites and Mechanics Laboratory (NCM Lab), University of New Brunswick, Fredericton, NB E3B 5A3, Canada

^b Alloy Design and Materials Testing Research Laboratory (AD-MTRL), University of New Brunswick, Fredericton, NB E3B 5A3, Canada

ARTICLE INFO

Keywords:
High-entropy alloy
AlCoCrFeNi
Nanoindentation
Phase fraction
Additive manufacturing

ABSTRACT

Particulate feedstock constitutes the building block in modern day additive manufacturing (AM) era. Cold spray (CS) is a leading process technology to adhere to the AM principle. Therefore, meeting feedstock qualities is of utmost interest to ensure the conformability and competitiveness of the developed industrial modules, including coatings, architectured components, and additively repaired devices. This research advances the understanding of nanoscale hardness/strength properties of particulate matters, specifically of an emerging material class, -high-entropy alloys (HEAs). The feasibility of determining the hardness of mechanically alloyed AlCoCrFeNi_x ($x = 0, 1, 2.1$) HEA particles was studied employing the nanoindentation technique. Mechanical properties of milled AlCoCrFeNi_x particles with varying Ni atomic ratio ($x = 0, 1, 2.1$) were investigated over different milling times ranging between 4 and 24 h. The study analyzed the impact of mounting resin, pre-determined maximum load, and indentation depth on hardness/strength properties. Results reveal that the hot mounted samples yielded greater accuracy and higher hardness values than compared to those of the cold mounted samples. Additionally, although the low-load sensitivity of AlCoCrFeNi_x provided consistent nano-scale hardness values across selected loads, their hardness values were found to be depth-dependent. Overall, the study concludes with a methodology for the nano-scale hardness/strength measurement of HEA particles that must account for particle size, sample preparation technique, and nanoindentation test parameters.

Introduction

The development of particulate feedstock with desirable qualities is one of the fundamental requirements for modern-day additive manufacturing technologies such as cold spraying (CS). With the wide range of potential applications of CS, including 2D/3D coatings, 3D/4D architectured components, and additively repaired or re-engineered devices, the success of the developed modules in CS relies on meeting the necessary particulate feedstock qualities, particularly mechanical properties. The applicability of the particulate feedstock is usually evaluated in terms of its hardness property since it can be correlated to the tensile strength of many metallic materials used for CS. In general, hardness is the material's ability to withstand permanent shape change or deformation under a constant compressive force. More importantly, hardness serves as an indicator of the material's wear resistance and ductility.

Numerous studies have already been performed to determine the

hardness property of metallic materials. While the application of micro-hardness determination techniques has been prevalent, most studies concentrate on bulk materials such as cast or deposited feedstock. Hardness determination for particulate feedstock is of equal importance with its bulk counterpart but is more challenging due to size limitations and very low-test forces required. The traditional hardness determination of particulate feedstock or powder usually involves post-processing by means of sintering which produces the sintered part or module. However, this additional process tends to induce extensive plastic deformation and work hardening, causing inaccuracy in the determined hardness of the particle [1].

With the advent of more sensitive and sophisticated instrumentation, hardness measurement has evolved from macro- and micro-scales to nano-scale level, from which the compressive forces or loads applied are controlled at milli-Newton (mN) to micro-Newton (μ N) range [2]. Known as nanoindentation, this method enables the accurate monitoring of the indentation depth and applied load during testing, having

* Corresponding author.

E-mail address: gsaha@unb.ca (G.C. Saha).

the indented area within a few micrometers to nanometer range. Consequently, the nanoindentation technique was proven to be highly effective in estimating the hardness of feedstock particles with sizes less than 100 μm . Moreover, it offers a significant advantage as it determines the size of the hardness impression from indenter force-displacement curves rather than relying on microscopic measurements of the residual hardness impression [3,4]. This unique capability enables researchers to explore and characterize the hardness of specimens to unprecedented small depths, even down to a few nanometers in some cases.

In the review made by Broitman [2], nanoindentation gained substantial momentum in 2015, to the extent that it has surpassed the interest in microhardness testing. To date, several studies investigated the application of nanoindentation to metallographic samples, noting its appropriateness for conducting material testing on thin films and bulk components [5–8]. While nanoindentation holds promise, its adoption in particle testing remains limited. In the recent study conducted by Slagter et al. [9], nanoindentation of embedded particles using the Oliver-Pharr method revealed that probing the properties of a particle embedded in a matrix with different elastic properties induces an extra (positive or negative) displacement. If not accounted for, this displacement can lead to inaccurate determination of both the elastic modulus and nanoindentation hardness.

This technique was found invaluable in understanding the distinctive attributes of bulk [10], coated [11], and thin film [12] high entropy alloy (HEA), particularly the dual-phase structured HEAs that offer improved strength-ductility balance, an area of significant interest for researchers due to its wide-ranging potential applications. High entropy alloy, a solid solution alloy that contains five or more elements with concentration range from 5 to 35 at%, is recognized to exhibit high hardness [13,14], high strength at elevated and cryogenic temperatures [15,16], and good wear and corrosion resistance [17–19].

AlCoCrFeNi HEA is one of the extensively investigated BCC systems for high-strength and high-temperature applications. The manufacturing routes explored to produce this alloy are either liquid-state processing such as casting or solid-state processing such as powder metallurgy which includes mechanical alloying. At a bulk scale, as in casted material, the incorporation of Ni to produce the AlCoCrFeNi alloy leads to a reduction in hardness and wear resistance [20]. This is attributed to the transformation of some BCC structures into more ductile FCC structures. On the other hand, AlCoCrFeNi_{2.1}, often referred to as eutectic high entropy alloy (EHEA), has emerged as a notable exception [21]. This alloy exhibits an excellent combination of strength and ductility.

The existing studies in HEA material characterization have contributed significantly to understand the bulk behavior and characteristics of the AlCoCrFeNi alloy system [22–25]. However, there remains a critical research gap in determining HEA mechanical properties when it is in particle condition. Despite the surge in popularity of nanoindentation in evaluating the hardness and strength of HEAs, the same limitations in indentation load and depth in particle testing were observed.

This paper presents the research data and discussions pertaining to the ongoing stride when it comes to evaluating nanoscale hardness of particles. The novelty of the work further lies in characterizing the nanoscale hardness properties of an emerging class of materials - high-entropy alloys (HEAs). To date, limited literature is available to assess the nanoscale hardness of HEA feedstock particles. Specifically, the study explored the feasibility of determining the nanoscale hardness of mechanically alloyed AlCoCrFeNi_x HEA particles with varying amounts of Ni ($x = 0, 1, 2.1$) through the nanoindentation technique with a Berkovich indenter. This research study contributes valuable insights into evaluating the nanoscale hardness of AlCoCrFeNi_x HEA feedstock particles and identifying the influence of feedstock processing and indentation on the measured hardness values.

Material and methodology

Powder preparation

AlCoCrFeNi_x ($x = 0, 1, 2.1$) feedstock samples were produced by milling elemental powders of Al, Co, Cr, Fe, and Ni with purity higher than 99% from Fisher Scientific, Canada. The milling process was carried out using a PQ series Gear Drive 4-station planetary ball milling machine, schematically shown in Fig. 1. To investigate the effect of milling time on the evolution of phases and hardness, different milling durations of 4, 12, and 24 h were employed at a constant rotation speed of 580 rpm, the details of which are found elsewhere [26]. Although other studies in HEA feedstock production take longer milling times [27, 28] depending on several factors, including the specific composition of the HEA, the milling equipment, and the desired properties to produce homogenous alloys, this study explores utilizing higher milling speed to reduce milling time. This is to prevent material contamination due to prolonged milling.

The design of experiment presented in Table 1 was used to synthesize HEA feedstock samples with varying Ni content and milling durations. By systematically studying the influence of these parameters on the phase transformations and hardness, valuable insights into the developed material's behavior and potential applications can be obtained.

Powder characterization

The free-standing samples of mechanically alloyed feedstock particles were analyzed for various characteristics, including morphology, particle size, and phase fraction. The particle morphology and composition before and after mechanical alloying were analyzed using a JEOL JSM 6010 scanning electron microscope (SEM) with energy-dispersive spectroscopy (EDS). Particle size distribution (PSD) testing was conducted using a Mastersizer Particle Size Analyzer. The analysis was performed on the as-received elemental powders and the developed HEA powders after 24 h of mechanical alloying for each Ni content variation. To study the phase evolution as milling time progressed for each Ni content variation, X-ray diffraction (XRD) patterns were acquired utilizing a Bruker D8 Advance spectrometer. The measurements covered the 5–90° (20) range, employing a step size of 0.02° and a 1-second step time. These XRD analyses were conducted under Cu-K α radiation (1.5406 Å) at 40 kV and 25 mA. The XRD peaks were identified using the Xpert Highscore® plus software. Additionally, XRD result was used to determine the volume phase fractions of the mechanically alloyed powders, which were selected from the peak intensities of the XRD patterns [10,28,29]. Refinements of all diffraction data were performed using the Rietveld method implemented in the FullProf software.

Nanoindentation of particles

Sample preparation

AlCoCrFeNi_x ($x = 0, 1, 2.1$) feedstock samples were prepared for nanoindentation testing as per the ATSM-E3 Standard Guide for Preparation of Metallographic Specimens, to ensure consistent and repeatable results. Samples were cold-mounted (CM) and hot-mounted (HM) via castable and compression mounting methods, respectively.

In the case of CM samples, the mechanically alloyed AlCoCrFeNi_x ($x = 0, 1, 2.1$) powders were loaded into a casting mold and affixed to the sample's surface using a resin composed of an epoxy-hardeners compound. The samples were allowed to set at room temperature for 24 h to allow the resin to properly harden. HM samples were prepared using Buehler SimpliMet™ 4000 under temperature and pressure cycle conditions of 350°F and 4200 psi, respectively, which are below the conditions that will affect the properties of any of the elements in the alloy. Samples were left to cure and cool under pressure and were ejected when completely cooled to ensure optimal results and minimize the risk of shrinkage gaps.

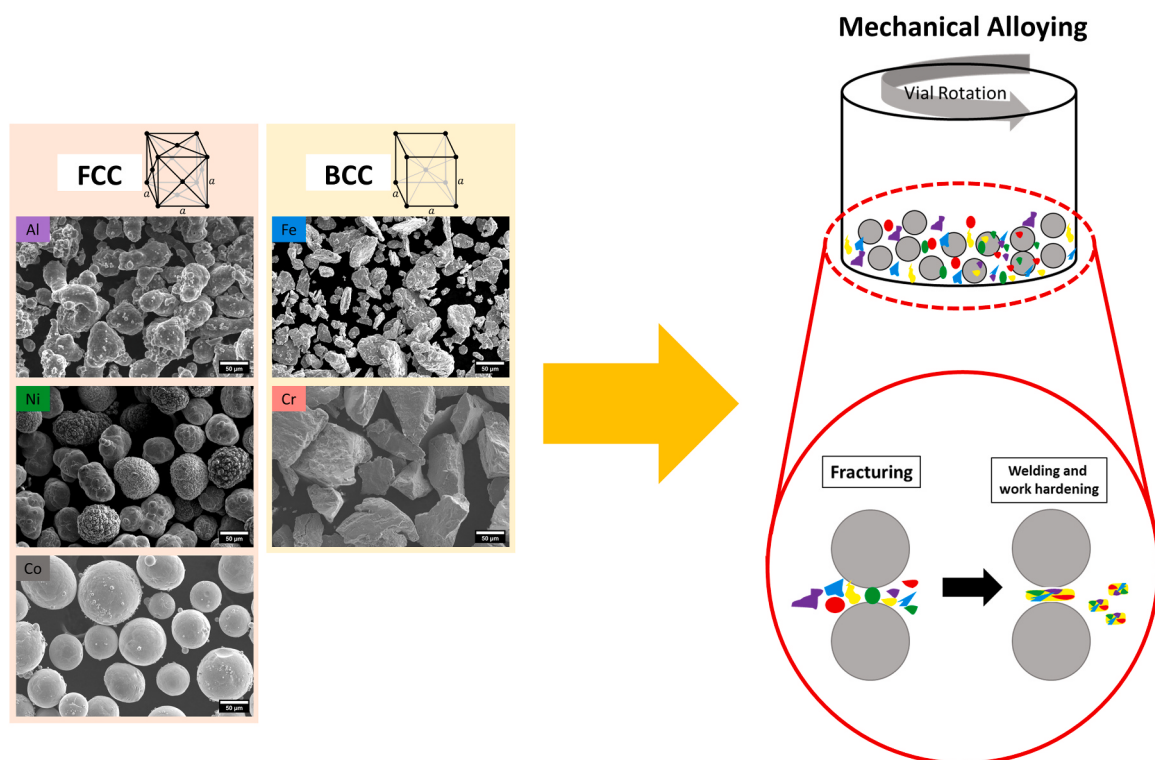


Fig. 1. Schematic diagram for the mechanical alloying of Al, Co, Cr, Fe, and Ni to produce AlCoCrFeNi_x ($x = 0, 1, 2.1$).

Table 1
Design of experiment for the preparation of AlCoCrFeNi_x ($x = 0, 1, 2.1$).

Designation	Alloy	Milling Time, hrs	Composition, wt%				
			Al	Co	Cr	Fe	Ni
A4	AlCoCrFe	4	13.93	30.42	26.84	28.82	0
A12		12					
A24		24					
B4	AlCoCrFeNi	4	10.69	23.34	20.60	22.12	23.25
B12		12					
B24		24					
C4	$\text{AlCoCrFeNi}_{2.1}$	4	8.57	18.73	16.52	17.75	38.43
C12		12					
C24		24					

After mounting, all samples were polished using a rotating wheel polisher (Pace Technologies NANO-1000S). This involves grinding with abrasive papers (800, 1000, and 1200 grit), and polishing using a 3-micron diamond abrasive suspension. The samples were polished to a mirror-like finish to minimize surface defects and ensure consistent results during nanoindentation testing [4].

Nanoindentation test

Hardness tests were conducted using a Nanomechanics Inc. iMicro™ Nanoindenter equipped with a Berkovich diamond indenter tip. Nanoindentation tests were performed at random locations across the face of the mounted powder samples for each set of testing parameters. Indentations were carried out on particles measuring less than 100 μm in size.

Indentation depths and loads were chosen such that the influence of the test piece support is not evident in the resulting hardness per ASTM E2546 Standard Practice for Instrumented Indentation Testing. The effect of mounting resin material was explored under various loading conditions (50, 100, 150, 350, and 500 mN) on the HM and CM samples. By using different resins as embedding media for the nanoindentation tests, their effects on the measured hardness values were evaluated. This

exploration helps in understanding the role of resin in supporting the particles during indentation and minimizing potential artifacts.

Indentation depths ranging from 750 to 3000 nm with a maximum loading value of 1000 mN were implemented on HM samples to investigate the variation of hardness with increasing indentation depths. By varying the indentation depth, the depth-dependent hardness behavior and potential indentation size effects (ISE) in the HEA system can be assessed. This analysis provides valuable information on the material's resistance to deformation at different depths.

To examine the correlation between hardness and applied loads, a series of tests using maximum loads of 50, 100, 150, 350, and 500 mN with constant 750 nm indentation depth were performed on CM samples. By varying the load applied during the nanoindentation test, the load sensitivity of the material can be examined. This investigation helps in understanding the deformation behavior and plasticity of the HEA particles under different loading conditions.

Oliver-Pharr method

The Oliver-Pharr nanoindentation method [30] is a technique developed in the 1990 s and used to measure the mechanical properties of materials at small scales, particularly the hardness and elastic

modulus [31]. The nano-scale nature of this method enables the use of experimental readings of indenter load and depth of penetration. These readings are employed to indirectly measure the contact area at full load; thus, enabling hardness calculations. Hardness measurements are based on the indentation area function and the maximum applied load, as depicted in Eq. 1. Throughout the loading and unloading segments of the nanoindentation testing, indentation load and depth are continuously recorded, providing insights into hardness as a function of depth beneath the surface.

$$H = \frac{P_{\max}}{A_{\max}} \quad (1)$$

where P_{\max} is the predetermined maximum load and A_{\max} is the indenter area at maximum load, related to the contact depth, h_c .

To determine the projected area of contact between the indenter and the specimen at maximum load, the precise measurement of contact depth into the specimen surface is employed in conjunction with the known indenter tip geometry [4]. Eq. 2 provides the relationship derived by Oliver-Pharr in their seminal work [32], employed to precisely quantify this parameter.

$$A_c = 24.5h_c^2 + C_1h_c + C_2h_c^{\frac{1}{2}} + C_3h_c^{\frac{1}{3}} + C_4h_c^{\frac{1}{4}} + C_5h_c^{\frac{1}{5}} + C_6h_c^{\frac{1}{6}} + C_7h_c^{\frac{1}{7}} + C_8h_c^{\frac{1}{8}} \quad (2)$$

where C_n ($n = 1-8$) are constants determined through precise curve fitting calibration procedures. The leading term characterizes a perfect (ideal) Berkovich indenter without defects, and the subsequent terms account for deviations from the ideal Berkovich tip [33].

Statistical analysis

Chauvenet's criterion [34] was utilized to assess the quality of the experimentally measured results. This method identifies and removes outliers through a systematic process involving the deviation calculation of samples via mean and standard deviation methods. Deviations exceeding a critical value threshold based on sample size, as provided in *Statistical Treatment of Experimental Data* [35], were eliminated. This method relies on the principle that the data exhibits a normal distribution, which is present in the experimental results of this study.

Corrected hardness computation

The experimental hardness values obtained from the nanoindenter were corrected based on the computation of Slagter et al. [9], by accounting for the extra compliance (ΔC) brought about by the elastic contribution of the matrix from which the particles are embedded. Computing for the corrected hardness values (H_{corr}) involves an iterative process starting initially with the particle elastic modulus (E_p) from the nanoindenter, which is considered as $E_{p,0}$. All the parameters and their corresponding values are presented in Table 2. The iteration starts with the computation of the ΔC (Eq. 3) using the value of $E_{p,0}$. This is followed by computing for the other parameters, such as the corrected hardness using Eqs. 4 to 6. The corrected elastic modulus, on the other hand, (E_r^{corr}) was computed using Eq. 6, which is then regarded as $E_{p,i}$ and was used to compute the new ΔC . The iterative computations were done until the value of $E_{p,i}$ converged with $E_{p,i+1}$. Lastly, the H^{corr} was computed from Eq. 7 using the corrected contact area (A_c^{corr}) from the iteration process.

$$\Delta C = \frac{\alpha}{D_p} \left(\frac{(1 - \nu_m^2)}{E_m} - \frac{(1 - \nu_p^2)}{E_p} \right) \quad (3)$$

$$S^{\text{corr}} = \left(\frac{1}{S} - \Delta C \right)^{-1} \quad (4)$$

$$h_c^{\text{corr}} = h_c - P\Delta C(1 - \epsilon) \quad (5)$$

Table 2

Parameters used for the iterative calculation of the corrected hardness.

Parameter	Symbol	Values Used	Units	Remarks
Proportionality constant	α	1.06	-	Simulated value for spherical particles from Slagter et al. [9]
Particle diameter	D_p	50	μm	Average particle size for AlCoCrFeNi _x ($x = 1$)
Particle elastic modulus	E_p	-	GPa	Values obtained from the nanoindenter for each trial [36]
Particle poisson's ratio	ν_p	0.3	-	
Matrix elastic modulus	E_m	14.156 (HM) 3.973 (CM)	GPa	Values obtained by indenting the actual resins used
Matrix poisson's ratio	ν_m	0.3	-	[37]
Stiffness	S	-	mN/μm	Values obtained for the derivative of the unloading curve of each trial
Contact depth	h_c	-	μm	Values were computed for each trial using $h_c = h_{\max} - \frac{P}{\epsilon S}$
Indentation load	P	-	mN	Values obtained from the nanoindenter for each trial
Indenter geometric constant	ϵ	0.75	-	Recommended value from Slagter et al. [9]
Correction factor	β	1.05	-	Recommended value from Slagter et al. [9]
Corrected contact area	A_c	-	μm ²	Values obtained using Eq. 2 as a function of the h_c^{corr} , on the assumption of a perfect indenter

$$E_r^{\text{corr}} = \frac{1}{\beta} \frac{S^{\text{corr}} \sqrt{\pi}}{2\sqrt{A_c^{\text{corr}}}} \quad (6)$$

$$H^{\text{corr}} = \frac{P}{A_c^{\text{corr}}} \quad (7)$$

Results and discussion

Particle size distribution and phase determination

As the milling time progressed, Al, Co, Cr, Fe, and Ni particles, as seen in Figs. 2a–2b representing the particle size distribution, underwent continuous fracturing and welding processes. This resulted in the formation of feedstock particles for a five-element high-entropy alloy, with the particle size being effectively controlled during the milling process. Fig. 2c shows the state of particles after 24 h of milling. It is evident that the mean particle size of AlCoCrFeNi_x ($x = 0, 1$, and 2.1) decreased to less than 50 μm due to the repeated mechanical deformation, fracturing, and welding of particles.

Interestingly, the mean particle size was found to be lower when Ni was introduced into the AlCoCrFe alloy system. However, as the atomic ratio of Ni increased from 1 to 2.1, the mean particle size increased to 35 μm. This behavior can be attributed to the presence of Ni atoms within the crystal lattice, which can impede the movement of dislocations responsible for plastic deformation. From a previous study of equiatomic bulk AlCoCrFeNi HEA, when the atomic ratio of Ni to other constituents, especially Al, is 1:1, the major composition of the alloy is BCC phase which exhibits high strength but inferior plasticity [38]. As the Ni atomic content increases to 2.1, FCC and BCC phases exhibit an excellent strength-plasticity synergy resulting in the conclusion that Ni-rich HEAs exhibit excellent overall strength and hardness of the material. Thus, in the case of AlCoCrFeNi HEA particles beyond the

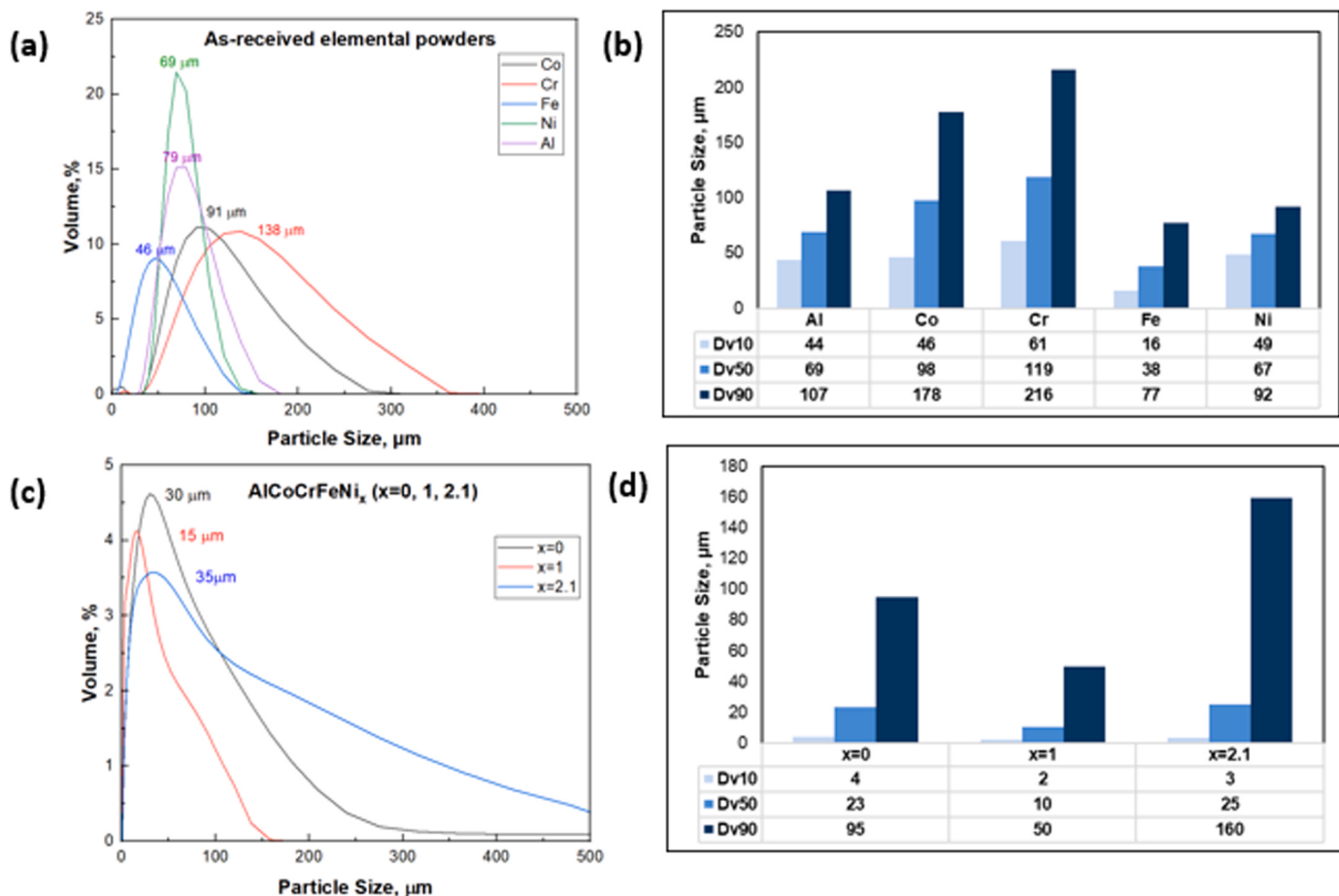


Fig. 2. Particle size distribution of (a)-(b) as received Al, Co, Cr, Fe, Ni powders, and (c)-(d) milled AlCoCrFeNi_x ($x = 0, 1, 2.1$) after 24 h of mechanical alloying.

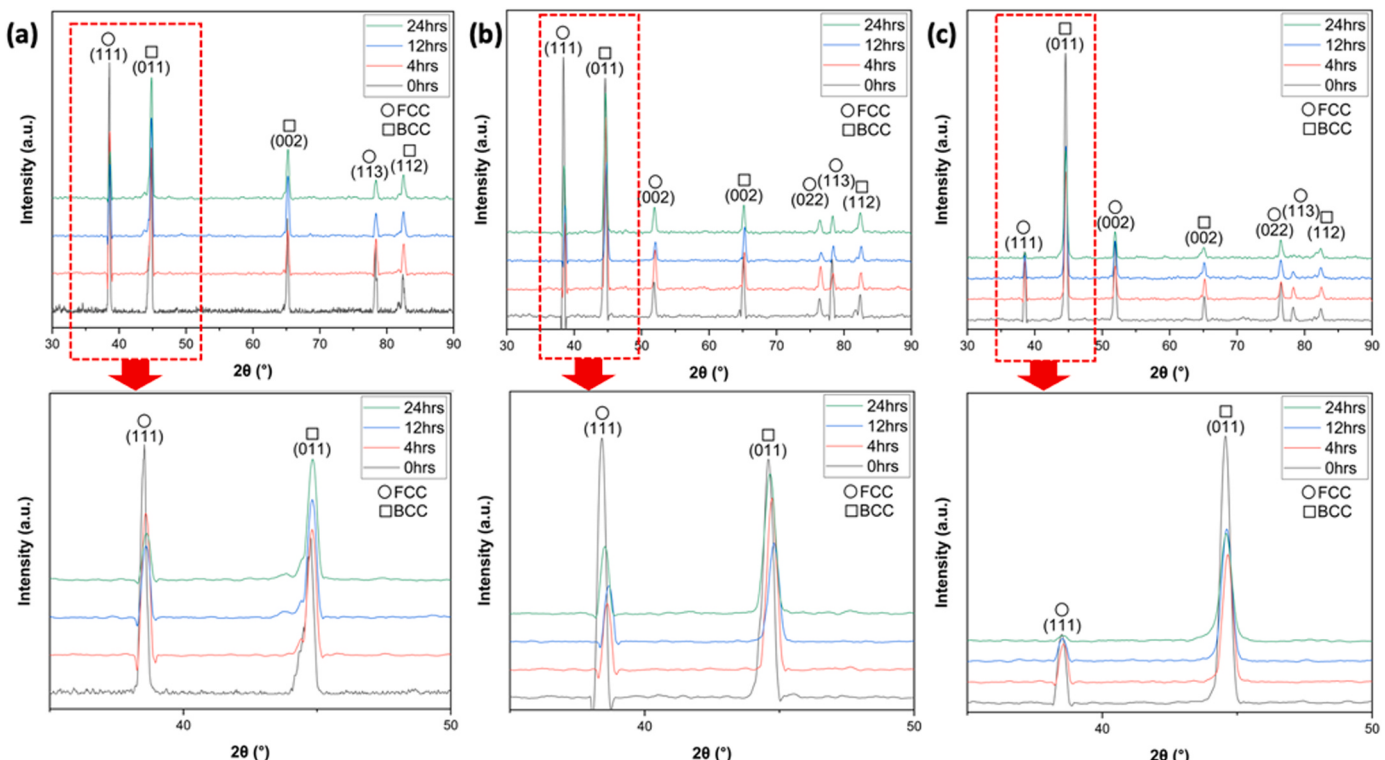


Fig. 3. XRD results of AlCoCrFeNi_x ($x = 0, 1, 2.1$) after 4, 12, and 24 h of mechanical alloying.

equiatomic ratio of Ni (i.e., $x = 2.1$), there is an improvement in ductility and toughness, limiting the fracturing during mechanical alloying and resulting in an increase in particle size, detailed in Fig. 2d.

The mechanical alloying process, which involves grinding powder mixtures in a high-energy ball mill, leads to significant phase transformation as the milling time progresses [39]. The repeated impact and grinding between balls and powder particles promote plastic deformation, fracturing, and cold welding of the particles. This process leads to the creation of nanocrystalline and/or an amorphous structure, making it an effective technique for producing HEAs. The mechanical alloying process, particularly when conducted in a planetary ball mill in this case, aims to produce HEAs with particle sizes less than 100 μm , suitable for CS applications. The milling parameters employed in this work have proven to be successful in achieving the desired particle size for the three HEA systems studied [26].

These findings highlight the effectiveness of mechanical alloying in producing HEAs with controlled particle sizes, opening up potential applications in various industries where the unique properties of HEAs are sought after for enhanced performance and functionality.

Fig. 3 illustrates phase transformation details during milling, where the crystallinity of the material is evident with the presence of FCC (face-centered cubic) and BCC (body-centered cubic) peaks after milling. In Fig. 3a, a shift in peak intensity of (111) and (011) peaks at $2\theta = 38.6^\circ$ and $2\theta = 44.8^\circ$, respectively, indicates a phase transformation from FCC to BCC phase after 12 h of milling AlCoCrFe.

In the case of AlCoCrFeNi, Fig. 2b shows only slight fluctuations in peak intensities as milling time progresses, and it seems that there is no formation of other intermetallics or contamination from milling media during mechanical alloying, as no new peaks appeared in the XRD patterns. This can be further verified by Transmission Electron Microscope (TEM) after feedstock was deposited via the cold spray process. Furthermore, the decrease in intensity of the FCC peak (111) and the disappearance of the peak (113) in Fig. 3c demonstrate the dissolution of the FCC phase, which is a positive indication of successful alloying.

The XRD patterns presented in Fig. 3 were analyzed using Eq. 8 for phase volume fraction, V_f , where I is the peak intensity of the phase and $\sum I_i$ is the total peak intensity of all phases in the XRD pattern [10,40]. Fig. 4 shows that the addition of Ni to the AlCoCrFe alloy system resulted in a slight increase in the BCC phase (46–54%) at the start of milling time (at 4 hrs). However, as the milling duration progressed from 4 to 24 h, a consistent proportion of ~50% BCC and ~50% FCC phases were seen and displayed in Fig. 4(x = 1). A slight decrease in the BCC phase of

AlCoCrFeNi ($x = 1$) was observed after 12 h of milling because of the presence of Ni resulting in the increase of the FCC phase as shown in the appearance of XRD peaks (002) and (022) in Fig. 3b. As milling time progresses to 24 h, the free energy of FCC may increase due to additional free energy supplied by dislocations making the BCC phase more stable. The phase fraction determined in this study for AlCoCrFeNi HEA feedstock after 24 h of milling (55% BCC phase and 45% FCC phase) was consistent with the phase fraction found on spark-plasma-sintered AlCoCrFeNi HEA (55.8% BCC/B2 phase and 44.2% FCC) with a hardness of 924 HV [10].

$$V_f = \frac{I}{\sum I_i} \times 100\% \quad (8)$$

As the Ni content increased further to an atomic ratio of $x = 2.1$, and the alloy system was milled for 4–24 h, an increasing phase fraction of BCC was observed. The trend of more BCC phase present in the HEA particles at higher milling time was seen on both AlCoCrFe and AlCoCrFeNi_{2.1} alloy systems. The incorporation of Ni, an FCC element, can improve the ductility of the material, and as milling time increases, the free energy of FCC may increase due to additional free energy supplied by dislocations. Consequently, making the BCC phase more stable (i.e., lower free energy state) and contributing to the increasing BCC phase in the alloy. A BCC structure is generally associated with higher hardness compared to other crystal structures. This is due to the lower atomic packing efficiency of the BCC structure, resulting in a higher density of dislocations and greater resistance to plastic deformation, leading to increased hardness.

In summary, the addition of Ni to the AlCoCrFe alloy system affected the crystal structure, and at certain atomic ratios, it led to a shift in the phase composition, favoring the formation of the BCC phase. This alteration in the crystal structure plays a crucial role in influencing the mechanical properties of the HEA particles. Understanding these phase changes is essential for tailoring the properties of HEAs and optimizing their performance for various applications, where increased hardness and resistance to plastic deformation are desired.

Influence of feedstock processing parameters on hardness

Milling time

As shown in Figs. 3 and 4, milling time can influence the phase composition of the material. As the milling time increases, some phases may undergo transformation, leading to changes in their mechanical properties. As shown in Fig. 5, the changes in phase composition can

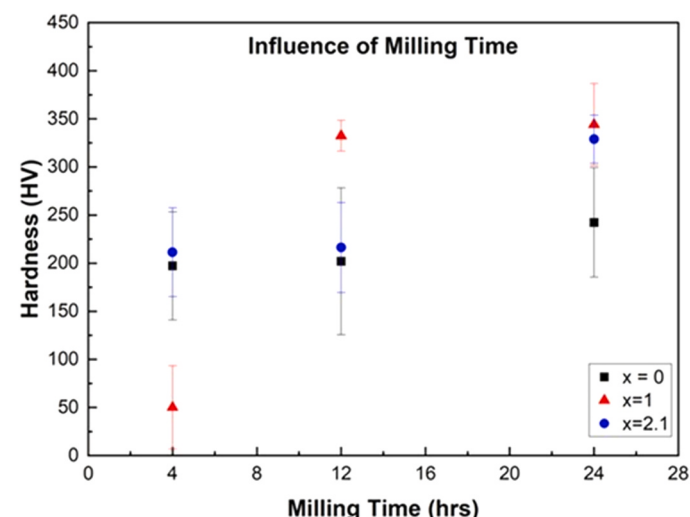


Fig. 5. Hardness of AlCoCrFeNi_x ($x = 0, 1, 2.1$) after 4, 12, and 24 h of mechanical alloying.

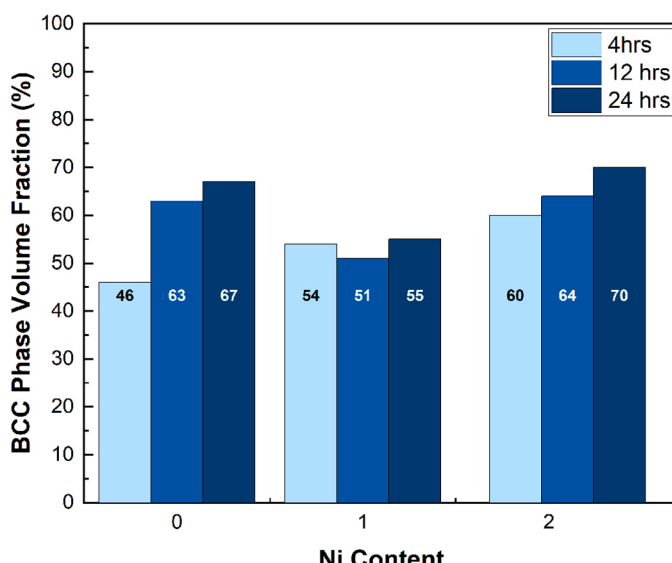


Fig. 4. BCC phase volume fraction of AlCoCrFeNi_x ($x = 0, 1, 2.1$) after 4, 12, and 24 h of mechanical alloying.

directly impact the hardness of the material. For instance, the formation of nanocrystalline phases or the transition from one crystal structure to another can significantly affect the material's mechanical properties [41]. Nanocrystalline phases typically have smaller grain sizes, higher dislocation densities, and altered grain boundaries, which can lead to increased hardness.

Furthermore, as milling time progresses, the accumulated deformation and dislocations generated during the mechanical alloying process can induce changes in the material's mechanical behavior. Throughout the alloying procedure, semi-coherent phase boundaries were formed due to the presence of chemically disordered distributions of multiple elements in HEA [42]. These strains influence the Gibbs energy of the system leading to phase evolution, all of which influence the hardness of the material as shown in Fig. 5. As the milling time of the three alloy systems increases from 4 h to 24 h, there is also an increase in hardness values. This shows that milling time is a critical parameter that influences the extent of strain accumulation and how prolonged mechanical alloying affects strain-induced phase changes and, consequently, material hardness.

Ni content

The hardness of an HEA system is influenced by both its composition and particle size. Each elemental composition within the HEA particle carries intrinsic properties that, when combined, lead to unique mechanical characteristics. In the AlCoCrFeNi alloy system, the addition of Ni resulted in lower hardness at the start of milling time but higher hardness values than AlCoCrFe alloy system as milling time progressed,

as evident from the results shown in Fig. 5. This can be attributed to the specific properties of Ni, which, when integrated into the alloy, enhances its hardness. Higher hardness is evident for high-entropy alloys with Ni atomic content of 1 and 2.1 presented in Fig. 5, measured at above 344 HV (3.64 GPa) and 370 HV (3.92 GPa), respectively.

While it might be expected that the hardness of AlCoCrFeNi would be lower than AlCoCrFe due to the decrease in the BCC phase (i.e., after 24 h), as illustrated in Fig. 4, the hardness values showed a reverse trend. This can be attributed to the presence of chemically disordered distributions of multiple elements in HEA, forming semi-coherent phase boundaries [42]. Although the BCC phase exhibited higher hardness, these phase boundaries effectively hindered dislocation movement, leading to the accumulation of dislocations within the FCC phase that led to high dislocation density. Consequently, a significant hardening of material is expected that is associated with the enhancement of strength despite the decrease in the proportion of BCC phase within this dual-phase material.

Additionally, as shown in Fig. 6, the morphology of AlCoCrFeNi_x HEA particles changed based on the Ni content. AlCoCrFe (Fig. 6a) appeared flat and more irregular in shape than AlCoCrFeNi (Fig. 6b), while AlCoCrFeNi_{2.1} (Fig. 6c) exhibited a flaky morphology after 24 h of mechanical alloying. The differences observed in particle shape have significant implications on the hardness results [43], considering that the particle diameter may not be uniform in different directions within the particle. Further in the discussion, the influence of nanoindentation parameters such as depth, load and resin type on sample thickness or length is highlighted.

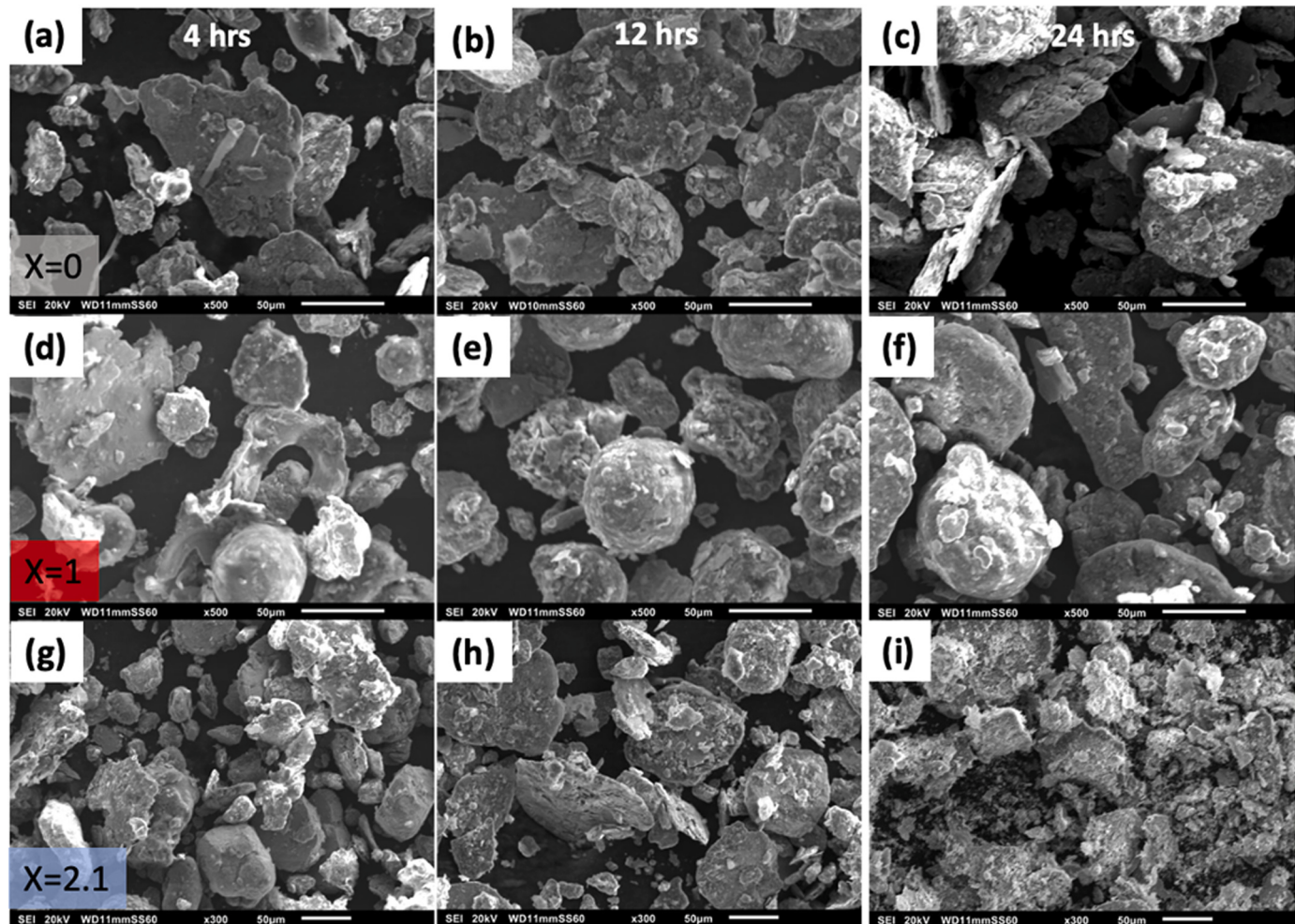


Fig. 6. SEM images of (a)-(c) AlCoCrFe, (d) – (f) AlCoCrFeNi, (g) – (i) AlCoCrFeNi_{2.1} feedstock particles after 4, 12 and 24 h of mechanical alloying.

Influence of indentation parameters on hardness

Mounting resin

The hardness test involves small indentations on the order of a few nanometers on the material's surface. The choice of mounting resin can influence the size and shape of the indentation due to differences in the mechanical properties of the resin compared to the sample. As a result, this factor can affect the calculated hardness values, as the indentation size is a critical parameter in hardness testing.

In this study, nanoindentation tests were carried out on mechanically alloyed feedstock samples of AlCoCrFeNi mounted by means of hot and cold mounting methods while progressively increasing the applied loads. The results revealed distinct trends between the two mounting methods, with HM AlCoCrFeNi feedstock samples consistently exhibiting higher hardness values compared to those metallographically prepared via the CM method. As the applied load increased, the average hardness of the HM samples exhibited fluctuations, ranging from 3.85 to 5.30 GPa, while the CM samples' hardness measured between 3.12 and 3.77 GPa. The percentage difference between the two mounting methods was calculated at each loading interval, the largest difference being 41% observed at 500 mN. The low hardness of CM samples at higher indentation load is due to the resin's low resistance to deformation. Additionally, Fig. 7 shows that the measured hardness of the CM AlCoCrFeNi samples in every indentation load fluctuated more, indicated by the larger coefficients of variation compared to the HM samples.

Powder consolidation is a fundamental method in powder metallurgy, which involves compacting loosely packed metal or alloy powder particles into a coherent structure for mechanical property testing. However, powder consolidation was deliberately omitted in this study prior to the mounting step and nanoindentation test. This is to prevent extensive plastic deformation and work hardening when transformation occurs from the loose particles to compact sample.

The CM method effectively attaches the metallographic powder within the resin, whereas the HM method involves subjecting the powders to compression at constant elevated pressures and temperatures to melt the resin granules leading to better adhesion between the powder particles and the mounting material. However, the HM process relies on the application of heat and high pressure to consolidate loose powders into a complete component. As heat is applied, the gaps between particles shrink, resulting in a denser product. The application of pressure compacts the powder particles further, thereby reducing the void space (or mean free path) among them. This reduction in void space can increase the resistance to deformation of the particles. Also, high-pressure

heat treatment generates high strains, inducing lattice distortion and increasing the density of dislocations. This, in turn, elevates the resistance to deformation [44]. Combined, the above factors contribute to higher measured hardness in HM samples. Thus, the temperature and pressure used during HM in this study are high enough to melt the resin powders but strategically lower than the temperature that will impact the properties of the HEA feedstock samples.

Both HM and CM resins demonstrate remarkably lower resistance to deformation, measuring the hardness at 0.25 GPa and 0.88 GPa, respectively, which are significantly lower than the hardness exhibited by the metallographic powders. The influence of the soft resin's matrix may alter the effective contact area between the indenter and the sample. As the powders are subjected to indentation, a more profound immersion of the HEA powders into the mounting resin occurs. When the indenter comes into contact with the mechanically alloyed feedstock particles, the HEA particles act as an indenter themselves, and the mounting medium may deform. As a result, the indenter experiences a greater displacement into the specimen, thus increasing the contact area and resulting in lower measured hardness values as evidenced by Eqs. 1 and 2.

A study conducted by Leggoe [43] reports similar findings in nanoscale hardness testing of embedded particles within a matrix exhibiting different elastic moduli. These findings are attributed to the impact of the mounting matrix, termed as the "secondary indentation" effect, which arises when stiffer indented particles are pressed into a more compliant matrix. Consequently, this secondary indentation induces additional penetration into the compliant matrix, dependent on its properties, as well as particle shape, dimension, and properties. As a result, the measured indentation depth tends to overestimate the actual depth of the particles, thereby influencing the recorded hardness values.

Slagter et al. [9] proposed modifications to the standard indentation method, presenting an adaptation of the Oliver-Pharr method to address the influence of the mounting resin matrix and the presence of a secondary indentation by restricting the depth of indentation. In Fig. 8, the corrected hardness values, accounting for the particle/matrix elastic inhomogeneity, are shown. It is noteworthy that these corrected hardness values in hot- and cold-mounted samples are higher by 0.10–0.40 GPa and 0.50–0.90 GPa, respectively, than those of the experimental results. The nanoindentation equipment used in this study employed the Oliver-Pharr method to generate nanoscale hardness data. However, it was found that this method underestimates the actual contact depth due to the pile-up phenomenon [45]. The proposed modifications by Slagter et al. (Section 2.3.5) were implemented to overcome this limitation and provide more accurate hardness measurements.

Indentation depth

During nanoindentation, the indenter penetrates the material surface to a certain depth, referred to as the indentation depth. It is established that when the material is indented, it responds by deforming elastically or plastically depending on the level of applied stress. In all indentation tests, plastic deformation zone was measured after elastic recovery [2]. Employing a shallower indentation depth in hardness testing results in relatively lower levels of deformation compared to its counterparts with larger indentation depths, as evidenced by larger hardness measurements based on Eq. 1. In this case, the indenter penetrates the material to a lesser extent, causing a smaller displacement or deformation zone and allowing for more elastic recuperation. The material near the surface experiences localized plastic deformation, resulting in a smaller volume of material being affected. On the other hand, when a deeper indentation depth is reached, the material undergoes more extensive deformation. Thus, this section presented how different depths of indentation influence the measured hardness values.

In investigating the mechanical properties of the mechanically alloyed AlCoCrFeNi feedstock samples after 24-hour milling, after considering the influence of mounting matrix, a clear dependence of

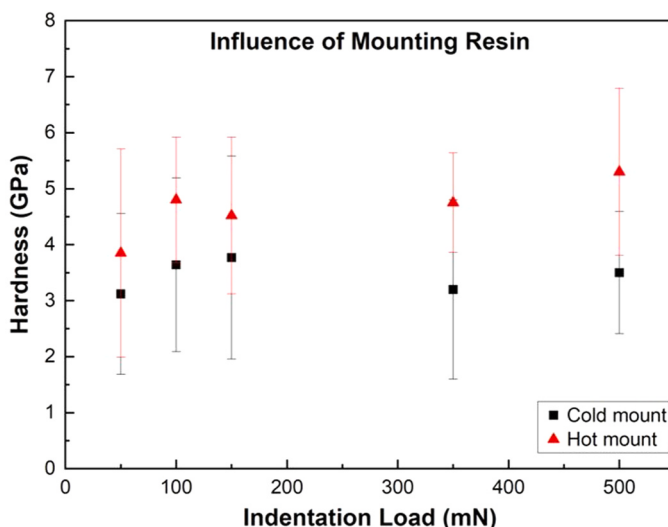


Fig. 7. Influence of mounting method on the hardness of AlCoCrFeNi_x (x = 1).

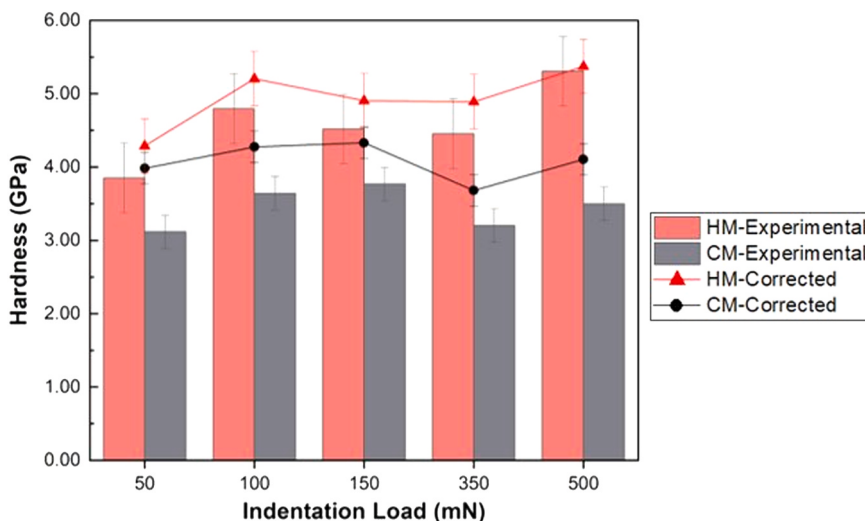


Fig. 8. Corrected hardness values for the HM and CM AlCoCrFeNi_x ($x = 1$) particles.

average hardness on the indentation depth is observed (represented by corrected hardness values), refer to Fig. 9. Notably, this trend is particularly evident when measuring at shallower depths. The results illustrate a gradual increase in average hardness as indentations become shallower. The trend of average hardness values, ascertained by systematically varying the indentation depth on the surface of AlCoCrFeNi_x (B24) samples is graphically depicted in Fig. 9.

The observed increase in hardness at shallow indentation depths (i.e., smaller contact area) can be attributed to the indentation size effect (ISE), which may greatly influence the interpretation of results. In essence, as observed by Tymiaik et al., ISE is a phenomenon when the hardness at shallow indentation depths is greater than those at deeper depths [46]. It arises from the fact that as the depth of indentation decreases to very small scales (typically in the nanometer range), the behavior of the material can deviate from the bulk properties. At shallower indentation depths, a larger portion of the material's response to the indenter is elastic in nature. As the indentation depth decreases, a greater proportion of the total deformation is absorbed elastically, meaning the material experiences less permanent or plastic deformation. The observed increase in hardness values is attributed to the increased reliance on elastic deformation to accommodate the stress induced by indentation. Specifically, at a depth of 750 nm, the material

exhibits a higher corrected hardness value of 3.83 GPa, whereas at a depth of 3000 nm, the corrected hardness value reduces to 1.78 GPa, as illustrated in Fig. 9.

Conversely, a further increase in indentation depth resulted in less contribution of elastic deformation. A larger volume of material experiences plastic deformation, resulting in a more extensive and homogeneous plastic zone around the indentation. As the plastic zone becomes dominant, the hardness value reaches a depth-independent constant value as observed in indentation depths of 2500 nm, and 3000 nm. This indicates that the material has undergone significant plastic deformation, and further increases in indentation depth do not significantly affect the hardness value [46].

Initially, the occurrence of ISE was attributed to measurement errors or surface preparation procedures. However, the most widely adopted model at the micrometer scale developed by Nix and Gao [47] showed that the geometrically necessary dislocations (GNDs) are generated during the indentation process to accommodate the volume of material displaced by the indenter, as illustrated in Fig. 10. These GNDs persist within a hemispherical plastic zone whose size is determined by the radius of indentation contact on the surface. The presence of GNDs plays a crucial role in the plastic deformation and mechanical behavior of materials, particularly at small scales. These dislocations significantly

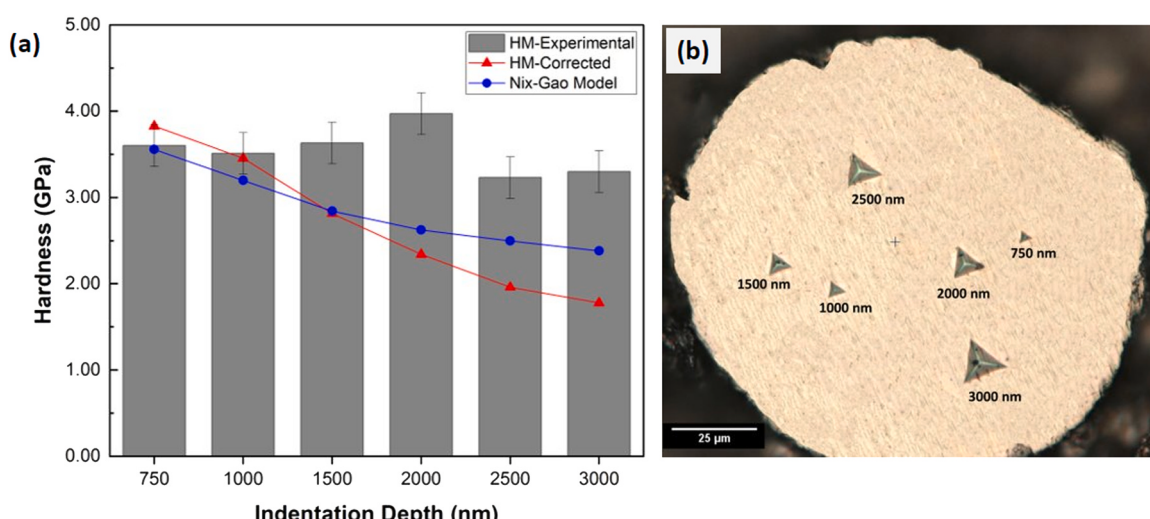


Fig. 9. (a) Influence of indentation depth on nano-scale hardness of AlCoCrFeNi_x ($x = 1$), and (b) particle micrograph with increasing indentation contact area as a function of indentation depth.

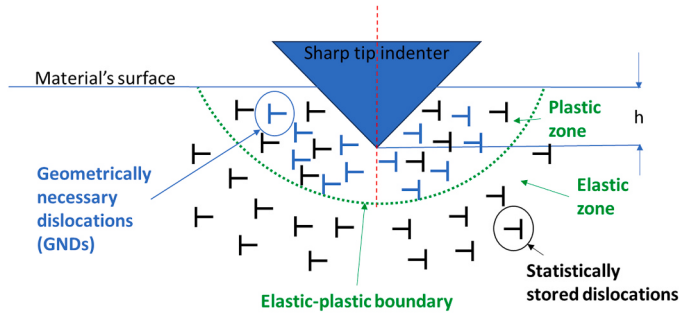


Fig. 10. Schematic diagram of GNDs generation during the indentation process.

impact material properties such as hardness, strength, and ductility by entangling and impeding further movement of existing dislocations (statistically stored dislocations), as well as the formation and movement of new dislocations.

Nix and Gao model, shown in Eq. 8, employed strain gradient plasticity showing dependence of the calculated hardness value on indentation depth for geometrically self-similar indenters [47,48]. As the indentation size decreases, the GND density increases, resulting in a higher hardness due to the interaction among dislocations, known as the Taylor hardening mechanism. The fundamental concept of Taylor hardening is that the dislocations formed during deformation act as obstacles to the motion of other dislocations [49]. These dislocations can take various forms, such as dislocation pile-ups, dislocation entanglements, and dislocation annihilation, all of which contribute collectively to the strengthening of material.

$$\frac{H}{H_o} = \sqrt{1 + \frac{h^*}{h}} \quad (9)$$

where H is the hardness for a given indentation depth, h ; H_o is the hardness in the limit of infinite depth; and h^* is a characteristic length that depends on the material and shape of the indenter tip.

In this study, the Nix-Gao model was employed to calculate the bulk-equivalent nanoindentation hardness from depth-dependent nanoindentation hardness [45]. By using this model, the relationship between the measured hardness during nanoindentation and the intrinsic hardness of the material was established. A linear relationship can be predicted between the square of hardness (H^2) and the inverse of depth ($1/h$). Fig. 9 presents the calculated hardness using the Nix-Gao model, indicating that at an indentation depth of 1500 nm, the value (2.84 GPa) aligns with the corrected experimental result (2.81 GPa). Thus, the corrected nanoindentation results obtained in this work showed that the hardness value of 2.81 GPa at an indentation depth of 1500 nm is the intrinsic hardness of AlCoCrFeNi HEA. Beyond this depth, the effect on hardness values is minimal, as evidenced by the insignificant changes observed.

The hardness tests conducted in this research utilized a sharp Berkovich tip, which is prismatic in shape. As a result, the measured hardness values inherently relied on the tip's geometry rather than being entirely dependent on the contribution of the indented material. In crystalline materials, when a pyramidal indenter is applied, the material undergoes deformation in the form of plastic and elastic responses. At shallow depths of penetration, the indenter encounters fewer atomic planes, leading to limited plastic deformation. As a result, the material exhibits higher values due to increased resistance to the indentation [50, 51].

In addition to understanding the ISE and its impact on nanoindentation hardness values, other practices have been implemented to mitigate the potential influence of indentation depth on the interpretation of results. The "10% rule" is a well-known practice in nano-scale hardness testing as it is aimed at minimizing the influence of substrate

properties on the measurement of coating properties by limiting the maximum depth of indentation. Its purpose is to restrict the plastic zone to the coating material to ensure accurate results. Fischer-Cripps discusses the relevance, validity, and limitations of this rule, emphasizing its importance in thin coating testing while acknowledging its applicability to the bulk material testing [52], such as relevant to this study. In essence, this rule ensures test piece thickness shall be large enough, or indentation depth small enough, such that the test result is not influenced by the test piece support. Test piece thickness should be at least 10 times the indentation depth or 6 times greater than the indentation radius; whichever is greater. This serves as a strong basis for nano-scale hardness testing, as it operates under the assumption that, if the indenter's penetration depth is less than 10% of the test piece thickness, the plastic zone resulting from indentation will be confined entirely within the test piece. Any elastic deformation from the substrate will have a negligible impact.

Overall, the experimentally obtained hardness values in this study, with consideration of the ISE are comparable to the published results of AlCoCrFeNi in bulk conditions (e.g., casted or coated) as shown in Fig. 11.

Indentation load

The influence of the indentation load on the hardness of the mechanically alloyed AlCoCrFeNi HEA particles with varying Ni content is presented in Fig. 12a. Initially, it is observed that the measured values for each indentation load were independent of each other, and specific trends can only be seen within certain ranges as the indentation load increases from 50 mN to 500 mN. For low indentation loads (50 and 100 mN), higher Ni content exhibited larger hardness measurements compared to the one without Ni. Increasing the indentation load from 150 to 350 mN showed some variations in the measured hardness. For $x = 0$ and $x = 2.1$, the hardness increased in the said range of indentation load, but the hardness decreased for $x = 1$. When the indentation load was further increased to 500 mN, the measured hardness values were contrary to the previous trend and found to be within the range of each other, as indicated by the error bars.

The variability of the measured hardness of the mechanically alloyed AlCoCrFeNi HEA particles can be attributed to the anisotropy induced by the distribution of phases (FCC and BCC) within the particle from which the indentation was done. Based on the XRD results presented in Fig. 3, FCC and BCC phases are present in the mechanically alloyed AlCoCrFeNi HEA particles. This is also evident for all alloys with varying

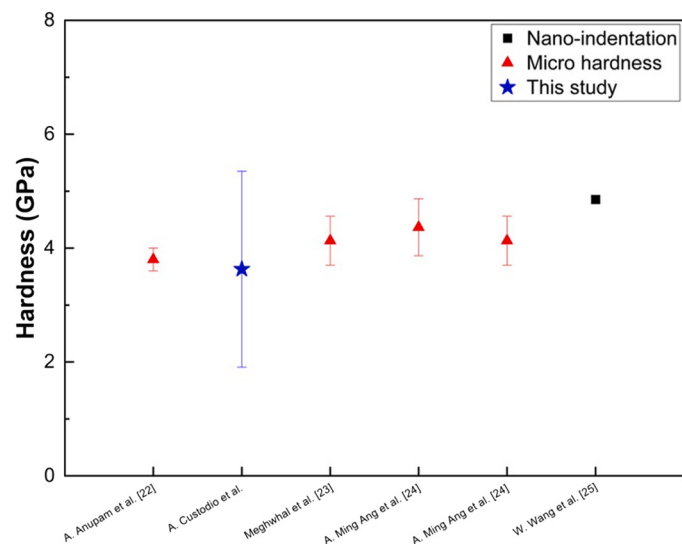


Fig. 11. Hardness results of AlCoCrFeNi feedstock particles in comparison to AlCoCrFeNi as coating and casted HEA.

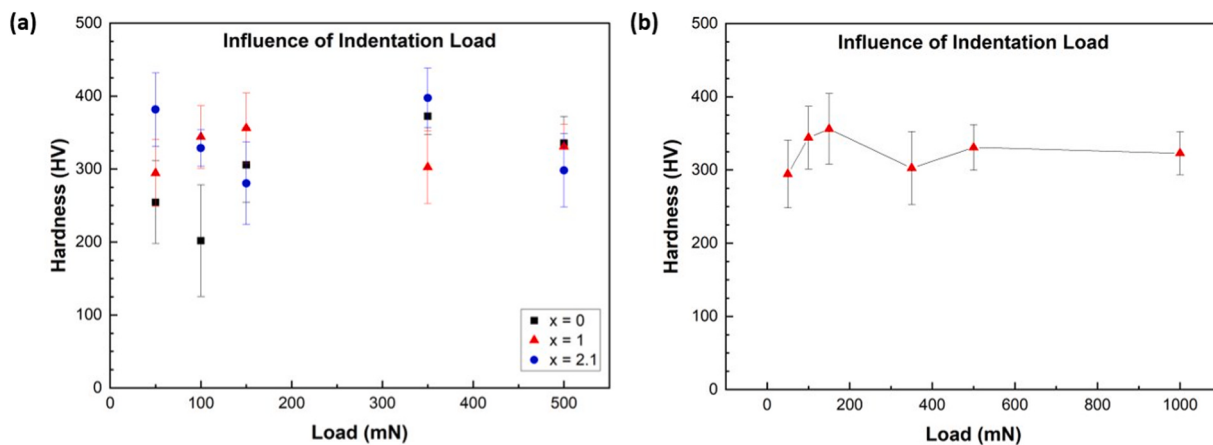


Fig. 12. Influence of indentation load on the nano-scale hardness of AlCoCrFeNi_x (a) for $x = 0, 1, 2.1$ from 50 to 500 mN; and (b) for $x = 1$ from 50 to 1000 mN.

Ni content ($x = 0, 1, 2.1$). At low indentation loads, the coverage of the indentation area has the possibility to focus only on regions with high phase volume fraction of either FCC or BCC. In relation to the measured hardness at low indentation loads, high hardness could mean that the indentation happened on a BCC phase-dominant region within the particle or in the semi-coherent phase boundaries.

Focusing on the influence of indentation load on the hardness for $x = 1$ (Fig. 12b), increasing the load from 500 to 1000 mN resulted in a relatively flat trend line in the graph. This behavior indicates that AlCoCrFeNi exhibits low load sensitivity, as there was minimal change in hardness with increasing load. Specifically, the measured hardness values for 500 and 1000 mN were almost the same, having a small standard deviation of ± 0.04 , which is more reliable than the measured hardness values for indentation loads less than 500 mN with a large standard deviation (± 0.27).

The consistency observed at higher indentation loads (500–1000 mN) can be attributed to the larger indentation area and a better FCC-BCC phase fraction distribution and can be considered as the load-independent range. Hence, the hardness measured at high indentation loads (for this study, up to 1000 mN) accurately represents the mechanical property of the mechanically alloyed AlCoCrFeNi HEA particles.

When different indentation loads are applied, the HEA particles experience varying levels of stress and strain during indentation. Higher

loads typically create a larger contact area between the indenter and the material, leading to increased plastic deformation, as evident from the larger indentation area for a given load in Fig. 13a. Conversely, lower loads induce less plastic deformation, resulting in a smaller indentation.

Despite the evident variation in indentation size as the indentation load was varied in Fig. 13a, the systematic variation of indentation loads showed a low load sensitivity of AlCoCrFeNi feedstock, as illustrated in a relatively flat trendline in Fig. 12. This finding highlights the material's ability to maintain consistent hardness measurement across a range of indentation loads. Furthermore, the loading-unloading curves at varying indentation loads for $x = 1$ in Fig. 13b, showing the indentation load as a function of indentation depth, indicate that the slopes of the unloading curves change without a specific trend. This behavior further supports the notion of low load sensitivity, as the changes in indentation load do not significantly affect the material's response during unloading.

Conclusions

In conclusion, this paper presents the viability of nanoindentation technique as a method to study the hardness/strength properties of AlCoCrFeNi_x ($x = 0, 1, 2.1$) HEA feedstock particles after mechanical alloying. The induced knowledge suggests that the reliability of the method is dependent on two sets of factors: 1) material specific and 2) test specific. The first factor combines the particle attributes such as

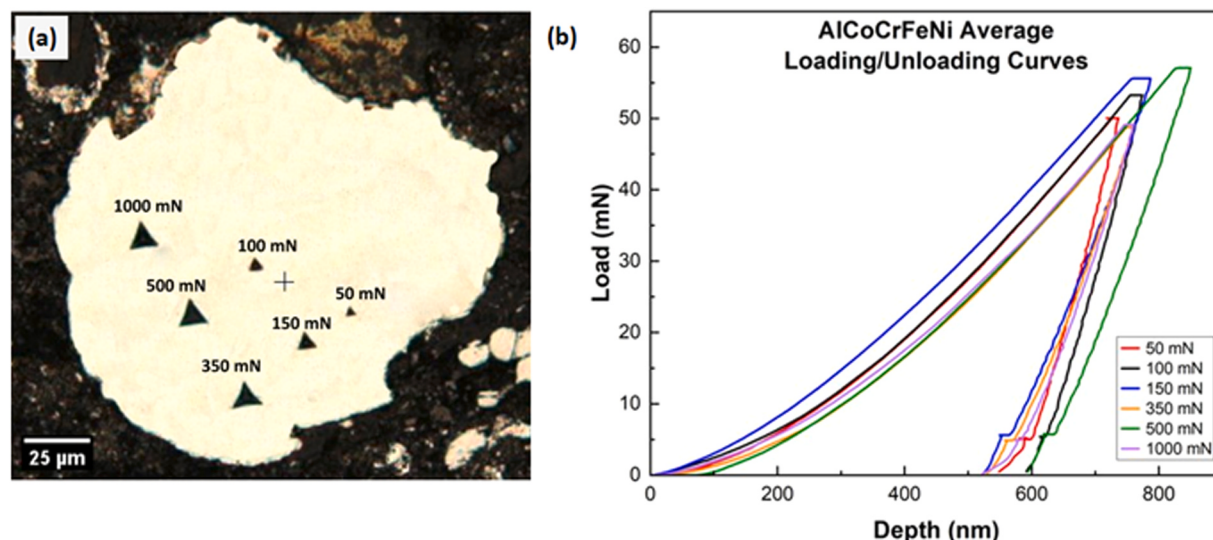


Fig. 13. (a) Micrograph of a particle with increasing indentation contact area as a function of indentation load, and (b) average loading and unloading curves for AlCoCrFeNi mechanically alloyed feedstock powders at varying indentation loads.

distribution of phase boundaries, size, and shape, whereas the test factor includes parameters such as mounting resin, indentation depth, and indentation load. The study yields the following significant conclusions:

- The nanoindentation technique is applicable to feedstock particle sizes in micrometer and nanometer size ranges as long as the sample is at least 10 times the indentation depth used. This ensures that any plastic zone resulting from indentation will be confined entirely within the test piece and the mounting resin has negligible impact.
- Based on corrected experimental hardness plots of hot- and cold-mounted samples at varying loads, there is a 0.10–0.90 GPa underestimation of hardness results. This is due to the lower deformation resistance of both hot and cold mounting resins which allows the indenter to displace further into the specimen, thus increasing the contact area and resulting in lower measured hardness values. Overall, the experimental hardness results of hot-mounted samples are higher than the cold-mounted samples and closer to the corrected values, considering the particle/matrix elastic inhomogeneity.
- The plot of the corrected hardness values of AlCoCrFeNi, obtained by varying indentation depth of 750–3000 nm using an adapted Oliver-Pharr method, revealed the presence of an Indentation Size Effect (ISE) indicating depth-dependence of AlCoCrFeNi HEA. Notably, the calculated hardness values using Nix-Gao demonstrated agreement with the corrected experimental results, particularly at an indentation depth of 1500 nm leading to the conclusion that the intrinsic hardness of AlCoCrFe HEA can be reliably determined at this specific indentation depth and measured to be 2.81 GPa.
- Based on a relatively flat trendline of hardness vs indentation load plot, AlCoCrFeNi demonstrates the material's low load sensitivity, indicating that the measured nano-hardness values are consistent across various indentation loads. However, a more consistent hardness values at 500 mN to 1000 mN showed the reliability of hardness measurements obtained at higher indentation loads to accurately represent its mechanical properties, creating larger indentation area to cover the semi-coherent phase boundaries formed due to the presence of chemically disordered distributions of multiple elements in HEA.

By considering the influence of particle size, sample preparation methods, and test parameters, accurate and consistent nanoindentation measurements were obtained, contributing to a deeper understanding of high-entropy alloy's acceptance as feedstock particles in CS applications.

Declaration of Competing Interest

The authors declare that they have no known competing financial interests or personal relationships that could have appeared to influence the work reported in this paper.

Data availability

The raw/processed data required to reproduce these findings cannot be shared at this time as the data also forms part of an ongoing study.

Acknowledgement

The authors acknowledge with gratitude funding received from the Natural Sciences and Engineering Research Council of Canada (NSERC; RGPIN-2018-04440, RGPIN-2019-04006), the Canada Foundation for Innovation (CFI; 38944), Transport Canada (CTS-R&D 15581129), the Atlantic Canada Opportunities Agency (ACOA; 220835), and the New Brunswick Innovation Foundation (NBIF; EP_2022_002).

References

- [1] E. Hryha, P. Zubko, E. Dudrová, L. Pešek, S. Bengtsson, An application of universal hardness test to metal powder particles, *J. Mater. Process. Technol.* vol. 209 (5) (2009) 2377–2385, <https://doi.org/10.1016/j.jmatprotec.2008.05.038>.
- [2] E. Broitman, Indentation hardness measurements at macro-, micro-, and nanoscale: a critical overview, *Tribol. Lett.* vol. 65 (1) (2016) 23, <https://doi.org/10.1007/s11249-016-0805-5>.
- [3] G.M. Pharr, E.G. Herbert, Y. Gao, The indentation size effect: a critical examination of experimental observations and mechanistic interpretations, *Annu. Rev. Mater. Res.* vol. 40 (1) (2010) 271–292, <https://doi.org/10.1146/annurev-matsci-070909-104456>.
- [4] A.C. Fischer-Cripps, *Nanoindentation. Mechanical Engineering Series*, Springer, New York, NY, 2011, <https://doi.org/10.1007/978-1-4419-9872-9>.
- [5] S. Bull, N. Moharrami, A comparison of nanoindentation pile-up in bulk materials and thin films, *Thin Solid Films* vol. 572 (2014) 189–199, <https://doi.org/10.1016/j.tsf.2014.06.060>.
- [6] S. Zak, C.O.W. Trost, P. Kreiml, M.J. Cordill, Accurate measurement of thin film mechanical properties using nanoindentation, *J. Mater. Res.* vol. 37 (7) (2022) 1373–1389, <https://doi.org/10.1557/s43578-022-00541-1>.
- [7] M. Cabibbo, Instrumented nanoindentation tests applied to bulk metallic materials: from calibration issue to Pile-Up Phenomena, *Materials* vol. 14 (21) (2021) 6360, <https://doi.org/10.3390/ma14216360>.
- [8] Y.-L. Shen, Nanoindentation for Testing Material Properties, in: S. Schmauder, C.-S. Chen, K.K. Chawla, N. Chawla, W. Chen, Y. Kagawa (Eds.), *Handbook of Mechanics of Materials*, Springer, Singapore, 2019, pp. 1981–2012, https://doi.org/10.1007/978-981-10-6884-3_46.
- [9] A. Slagter, J. Everaerts, A. Mortensen, Nanoindentation of embedded particles | SpringerLink Feb. 10, 2023, <https://link.springer.com/article/10.1557/s43578-023-00920-2> (accessed July 21, 2023).
- [10] M.C. Oh, A. Sharma, H. Lee, B. Ahn, Phase separation and mechanical behavior of AlCoCrFeNi-X (X = Cu, Mn, Ti) high entropy alloys processed via powder metallurgy, *Intermetallics* vol. 139 (2021), 107369, <https://doi.org/10.1016/j.intermet.2021.107369>.
- [11] M. Dada, P. Popoola, N. Mathe, S. Adeosun, S. Pityana, Investigating the elastic modulus and hardness properties of a high entropy alloy coating using nanoindentation, *Int. J. Lightweight Mater. Manuf.* vol. 4 (3) (2021) 339–345, <https://doi.org/10.1016/j.ijlmm.2021.04.002>.
- [12] Y.P. Cai, G.J. Wang, Y.J. Ma, Z.H. Cao, X.K. Meng, High hardness dual-phase high entropy alloy thin films produced by interface alloying, *Scr. Mater.* vol. 162 (2019) 281–285, <https://doi.org/10.1016/j.scriptamat.2018.11.004>.
- [13] Y. Zhang, et al., Microstructures and properties of high-entropy alloys, *Prog. Mater. Sci.* vol. 61 (2014) 1–93, <https://doi.org/10.1016/j.pmatsci.2013.10.001>.
- [14] P. Edalati, A. Mohammadi, M. Katabchi, K. Edalati, Ultrahigh hardness in nanostructured dual-phase high-entropy alloy AlCrFeCoNiNb developed by high-pressure torsion, *J. Alloy. Compd.* vol. 884 (2021), 161101, <https://doi.org/10.1016/j.jallcom.2021.161101>.
- [15] A. Gali, E.P. George, Tensile properties of high- and medium-entropy alloys, *Intermetallics* vol. 39 (2013) 74–78, <https://doi.org/10.1016/j.intermet.2013.03.018>.
- [16] J. Qiao, S. Ma, E.-W. Huang, C.P. Chuang, P. Liaw, Y. Zhang, Microstructural characteristics and mechanical behaviors of AlCoCrFeNi high-entropy alloys at ambient and cryogenic temperatures, *Mater. Sci. Forum* vol. 688 (2011) 419–425, <https://doi.org/10.4028/www.scientific.net/MSF.688.419>.
- [17] M.-H. Chuang, M.-H. Tsai, W.-R. Wang, S.-J. Lin, J.-W. Yeh, Microstructure and wear behavior of AlxCo1.5CrFeNi1.5Ti high-entropy alloys, *Acta Mater.* vol. 59 (16) (2011) 6308–6317, <https://doi.org/10.1016/j.actamat.2011.06.041>.
- [18] P. Lu, et al., Computational materials design of a corrosion resistant high entropy alloy for harsh environments, *Scr. Mater.* vol. 153 (2018) 19–22, <https://doi.org/10.1016/j.scriptamat.2018.04.040>.
- [19] C. Lee, Y.-Y. Chen, C. Hsu, J.-W. Yeh, H. Shih, The effect of boron on the corrosion resistance of the high entropy alloys Al_[sub 0.5]CoCrCuFeNiB_[sub x], *J. Electrochem. Soc.* vol. 154 (2007) C424–C430, <https://doi.org/10.1149/1.2744133>.
- [20] R.K. Sim, Z. Xu, M.Y. Wu, A. He, D.L. Chen, D.Y. Li, Microstructure, mechanical properties, corrosion and wear behavior of high-entropy alloy AlCoCrFeNi and medium-entropy alloy, *J. Mater. Sci. Jun.* (2022), <https://doi.org/10.1007/s10853-022-07256-y>.
- [21] J. Charkhchian, A. Zarei-Hanzaki, A. Moshiri, H.R. Abedi, T.M. Schwarz, R. Lawitzki, G. Schmitz, K. Chadha, C. Aranas Jr, J. Shen, J.P. Oliveira, Spinodal decomposition of B₂-phase and formation of Cr-Rich nano-precipitates in AlCoCrFeNi_{2.1} eutectic high-entropy alloy, *Adv. Eng. Mater.* vol. 25 (16) (2023) 2300164, <https://doi.org/10.1002/adem.202300164>.
- [22] A. Anupam, S. Kumar, N.M. Chavan, B.S. Murty, R.S. Kottada, First report on cold-sprayed AlCoCrFeNi high-entropy alloy and its isothermal oxidation, *J. Mater. Res.* vol. 34 (5) (2019) 796–806, <https://doi.org/10.1557/jmr.2019.38>.
- [23] A. Meghwal, A. Anupam, V. Luzin, C. Schulz, C. Hall, B.S. Murty, R.S. Kottada, C. C. Berndt, A. Siau Ming Ang, Multiscale mechanical performance and corrosion behaviour of plasma sprayed AlCoCrFeNi high-entropy alloy coatings, *J. Alloy. Compd.* vol. 854 (2021), 157140, <https://doi.org/10.1016/j.jallcom.2020.157140>.
- [24] A.S.M. Ang, C.C. Berndt, M.L. Sesso, A. Anupam, Praveen S, R.S. Kottada, B. S. Murty, Plasma-sprayed high entropy alloys: microstructure and properties of AlCoCrFeNi and MnCoCrFeNi, *Metall. Mater. Trans. A: Phys. Metall. Mater. Sci.* vol. 46 (2) (2015) 791–800, <https://doi.org/10.1007/s11661-014-2644-z>.
- [25] W.-R. Wang, W.-L. Wang, S.-C. Wang, Y.-C. Tsai, C.-H. Lai, J.-W. Yeh, Effects of Al addition on the microstructure and mechanical property of Al xCoCrFeNi high-

- entropy alloys, *Intermetallics* vol. 26 (2012) 44–51, <https://doi.org/10.1016/j.intermet.2012.03.005>.
- [26] A.G. Custodio, G.C. Saha, C. Aranas Jr, “Design, synthesis, and characterization of single- and dual-phase, equiatomic high entropy alloy particles through conventional and novel sequential mechanical alloying method,” *Powder Technology*, Submitted for publication, 2023.
- [27] M. Ghanbariha, M. Farvizi, T. Ebadzadeh, Microstructural development in nanostructured AlCoCrFeNi-ZrO₂ high-entropy alloy composite prepared with mechanical alloying and spark plasma sintering methods, *Mater. Res. Express* vol. 6 (12) (2019) 1265b5, <https://doi.org/10.1088/2053-1591/ab5fc9>.
- [28] F. Leitão Muniz, M. Miranda, C. Morilla-Santos, J. Sasaki, The Scherrer equation and the dynamical theory of X-ray diffraction, *Acta Crystallogr. Sect. A Found. Adv.* vol. 72 (2016) <https://doi.org/10.1107/S205327331600365X>.
- [29] L. Nath, G.C. Saha, Synthesis and characterization of nanocrystalline Al₂O₃-Ni(Cr) particles using high-energy mechanical alloying process, *Surf. Coat. Technol.* vol. 318 (2017) 262–269, <https://doi.org/10.1016/j.surfcoat.2017.01.024>.
- [30] W.C. Oliver, G.M. Pharr, An improved technique for determining hardness and elastic modulus using load and displacement sensing indentation experiments, *J. Mater. Res.* vol. 7 (6) (1992) 1564–1583, <https://doi.org/10.1557/JMR.1992.1564>.
- [31] P. Sudharshan Phani, W.C. Oliver, G.M. Pharr, Measurement of hardness and elastic modulus by load and depth sensing indentation: improvements to the technique based on continuous stiffness measurement, *J. Mater. Res.* vol. 36 (11) (2021) 2137–2153, <https://doi.org/10.1557/s43578-021-00131-7>.
- [32] W.C. Oliver, G.M. Pharr, Measurement of hardness and elastic modulus by instrumented indentation: advances in understanding and refinements to methodology, *J. Mater. Res.* vol. 19 (1) (2004) 3–20, <https://doi.org/10.1557/jmr.2004.19.1.3>.
- [33] J.P. Campbell, A. Astarita, A. Viscusi, G.C. Saha, Investigation of strain-hardening characteristics of cold-sprayed Al-Al₂O₃ coatings: a combined nanoindentation and expanding cavity models approach, *Surf. Eng.* vol. 36 (10) (2020) 1022–1031, <https://doi.org/10.1080/02670844.2019.1620438>.
- [34] D. Bayless, “Statistical Rejection of ‘Bad’ Data - Chauvenet’s Criterion.” 2005. (Accessed: Jul. 05, 2023.) [Online]. Available: <https://chetaero.files.wordpress.com/2016/11/chauvenet.pdf>.
- [35] H.D. Young, Statistical Treatment of Experimental Data, McGraw-Hill, 1962 ([Online]. Available) <https://www.nhn.ou.edu/~johnson/Education/Juniorlab/TEXT/StatisticalTreatmentofData-HughDYoung-All.pdf>.
- [36] Z.-M. Jiao, S.-G. Ma, G.-Z. Yuan, Z.-H. Wang, H.-J. Yang, J.-W. Qiao, Plastic deformation of Al_{0.3}CoCrFeNi and AlCoCrFeNi high-entropy alloys under nanoindentation, *J. Mater. Eng. Perform.* vol. 24 (8) (2015) 3077–3083, <https://doi.org/10.1007/s11665-015-1576-0>.
- [37] H. Yamaguchi, T. Enomoto, T. Fujita, Measurement of Poisson’s Ratio of Resin Materials in 2021 IEEE CPMT Symposium Japan (ICSJ), Nov. 2021, pp. 65–68. <https://doi.org/10.1109/ICSJ52620.2021.9648901>.
- [38] Q.W. Tian, G.J. Zhang, K.X. Yin, W.L. Cheng, Y.N. Wang, J.C. Huang, Effect of Ni content on the phase formation, tensile properties and deformation mechanisms of the Ni-rich AlCoCrFeNix (x = 2, 3, 4) high entropy alloys, *Mater. Charact.* vol. 176 (2021), 111148, <https://doi.org/10.1016/j.matchar.2021.111148>.
- [39] M. Vaidya, M. Garlapati, B. Murty, High-entropy alloys by mechanical alloying: a review, *J. Mater. Res.* vol. 34 (2019) 664–686, <https://doi.org/10.1557/jmr.2019.37>.
- [40] A. Shabani, M.R. Toroghinejad, A. Shafiei, R.E. Logé, Microstructure and mechanical properties of a multiphase FeCrCuMnNi high-entropy alloy, *J. Mater. Eng. Perform.* vol. 28 (4) (2019) 2388–2398, <https://doi.org/10.1007/s11665-019-04003-4>.
- [41] V. Maier, C. Schunk, M. Göken, K. Durst, Microstructure-dependent deformation behaviour of bcc-metals – indentation size effect and strain rate sensitivity, *Philos. Mag.* vol. 95 (16–18) (2015) 1766–1779, <https://doi.org/10.1080/14786435.2014.982741>.
- [42] Q. Wang, Y. Lu, Q. Yu, Z. Zhang, The exceptional strong face-centered cubic phase and semi-coherent phase boundary in a eutectic dual-phase high entropy alloy AlCoCrFeNi (Art. no), *Sci. Rep.* vol. 8 (1) (2018) 1, <https://doi.org/10.1038/s41598-018-33330-0>.
- [43] J.W. Leggoe, “Determination of the elastic modulus of microscale ceramic particles via nanoindentation | SpringerLink,” Aug. 01, 2004. <https://link.springer.com/article/10.1557/JMR.2004.0300> (accessed Jul. 21, 2023).
- [44] T. Gu, et al., Effect of high temperature-high pressure treatment on microstructure and mechanical properties of Cu-Cr alloy, *Mater. Res. Express* vol. 7 (2) (2020), 026505, <https://doi.org/10.1088/2053-1591/ab6c10>.
- [45] D. Geng, H. Yu, S. Kondo, R. Kasada, Toward the correlation of indentation hardness in micro- and nano-scale: understanding of indentation edge behaviors in Fe-Cr alloys, *J. Mater. Sci.* vol. 57 (28) (2022) 13736–13755, <https://doi.org/10.1007/s10853-022-07461-9>.
- [46] N.I. Tymlak, D.E. Kramer, D.F. Bahr, T.J. Wyrobek, W.W. Gerberich, Plastic strain and strain gradients at very small indentation depths, *Acta Mater.* vol. 49 (6) (2001) 1021–1034, [https://doi.org/10.1016/S1359-6454\(00\)00378-5](https://doi.org/10.1016/S1359-6454(00)00378-5).
- [47] W.D. Nix, H. Gao, Indentation size effects in crystalline materials: a law for strain gradient plasticity, *J. Mech. Phys. Solids* vol. 46 (3) (1998) 411–425, [https://doi.org/10.1016/S0022-5096\(97\)00086-0](https://doi.org/10.1016/S0022-5096(97)00086-0).
- [48] X. Ma, W. Higgins, Z. Liang, D. Zhao, G.M. Pharr, K.Y. Xie, Exploring the origins of the indentation size effect at submicron scales, *Proceedings of the National Academy of Sciences*, vol. 118, no. 30, p. e2025657118, Jul. 2021, <https://doi.org/10.1073/pnas.2025657118>.
- [49] G.I. Taylor, The mechanism of plastic deformation of crystals. Part I.—Theoretical, *Proc. R. Soc. Lond. A* vol. 145 (855) (1934) 362–387, <https://doi.org/10.1098/rspa.1934.0106>.
- [50] A.K. Kampouris, A.A. Konstantinidis, On the interpretation of the indentation size effect (ISE) through gradient theory for Vickers and Berkovich indenters, *J. Mech. Behav. Mater.* vol. 25 (5–6) (2016) 161–164, <https://doi.org/10.1515/jmbm-2017-0003>.
- [51] J.G. Swadener, E.P. George, G.M. Pharr, The correlation of the indentation size effect measured with indenters of various shapes, *J. Mech. Phys. Solids* (2002).
- [52] A.C. Fischer-Cripps, Critical review of analysis and interpretation of nanoindentation test data (Apr), *Surf. Coat. Technol.* vol. 200 (14) (2006) 4153–4165, <https://doi.org/10.1016/j.surfcoat.2005.03.018>.